Journal of Sound and Vibration (1999) **221**(4), 709–732
Article No. jsvi.1998.2038, available online at http://www.idealibrary.com on IDEAL

MODELLING, SIMULATION AND EXPERIMENTAL VERIFICATION OF CONTACT/IMPACT DYNAMICS IN FLEXIBLE MULTI-BODY SYSTEMS

S. HARIHARESAN AND A. A. BARHORST
Department of Mechanical Engineering, *Texas Tech University*, *Lubbock*, *TX* 79409-1021, *U.S.A.*

(*Received* 4 *June* 1998, *and in final form* 9 *November* 1998)

Contact/impact in flexible multibody systems that undergo pre-contact free motion, contact/impact and post-impact constraint motion is modelled. The shortcomings of using coefficients of restitution, penalty parameters and Lagrange multipliers are overcome by using a methodology for modelling non-holonomic hybrid parameter multiple body systems (HPMBS). The minimum set of equations required for the systems were developed using the methodology. All the dynamics of the manipulator (elaborated in the section below) are modelled with very few degrees of freedom. The model was experimentally validated via a planar two-link flexible manipulator that undergoes the complete motion regime. The comparisons show that the model predicts the complete dynamics of the manipulator accurately and the transition between the different modes of motion is seamless.

1. INTRODUCTION

Contact/impact in multibody and flexible multibody systems is of prime interest and is under current study by many researchers. The most common techniques used to model such systems are the Newtonian, Lagrangian and Hamiltonian methods. In the case of non-holonomic multi-body systems, the Lagrangian formulation requires the use of Lagrange multipliers which introduce additional algebraic equations. These additional equations tend to make the system of equations numerically more difficult to solve. Also, the formulation does not provide the minimum set of equations for the system. The Newtonian method has the advantage of vectorial formulation but gets extremely tedious in the case of multibody systems. The large amount of work that has to be expended in developing the equations of motion for flexible multibody systems using the above methods has been documented by Barhorst [1]. To overcome the difficulties mentioned above, a methodology based on the Kane's form of the Gibbs–Appel equations that is direct and easily applicable was presented by Barhorst [1, 2].

0022–460X/99/040709 + 24 $30.00/0

The impact process, in most cases, is modelled using a coefficient of restitution derived using kinematic, kinetic or energy based formulations [3]. As documented by Brach, there are some inconsistencies when using such coefficients of restitution, especially in the case of eccentric collisions where, in some instances an increase in energy has been observed. Stronge [4] has shown that an improper treatment of the kinematic coefficient of restitution can lead to such energy gains. Stoianovici and Hurmuzulu [5] show the effect of incident angle on the coefficient of restitution and also show that using a constant restitution coefficient leads to incorrect results in the case of oblique impacts. They derive a slenderness ratio, and through experiments show that only for rods with relatively low slenderness ratio, the coefficient of restitution remains almost invariant throughout the range of incident angles. In the case where penalty methods are used to satisfy the contact constraint, the problem of interpenetration cannot be avoided. If the contact constraint violation is to be avoided, then a large penalty parameter has to be used which leads to numerical instabilities [6, 7]. When Lagrange multipliers are used to enforce the surface contact displacement constraint, the problems discussed above w.r.t. Lagrange multipliers have to be dealt with.

A methodology for modelling hybrid-parameter multiple body systems (HPMBS) was presented by Barhorst [1, 2, 8, 9] to overcome the above mentioned inadequacies. The process of contact/impact is modelled through an instantaneously applied non-holonomic constraint where the need for the use of a coefficient of restitution, a penalty parameter or a Lagrange multiplier is eliminated. The contact constraint is also completely satisfied. In the work presented, the authors implicitly neglect the elastic deformation of the rigid bodies in the region of impact as it is assumed that most of the energy on impact goes into deforming the elastic bodies. Although the macroscopic motion of the system of bodies was modelled, the elastic effects are predicted with a great degree of accuracy.

This paper is devoted to experimentally verifying the methodology presented by Barhorst [1, 2] and uses the algorithm presented in reference [9]. The model, a two-link flexible manipulator, to be verified will encompass the complete motion regime, namely pre-contact free motion, contact/impact and post-impact constraint motion. It will also include friction on impact, in constrained motion, effect of all interconnecting rigid bodies, i.e., rigid bodies that connect the elastic bodies to the drive mechanism, etc., dynamics of driving motors and gearboxes and the effect of backlash of gearboxes. As mentioned earlier no coefficient of restitution is used.

The mathematical model is presented in the next section. Discussed in section 3.2 are the experimental set-up and the comparison of experimental and simulation results. The final section is the summary of the results.

2. MATHEMATICAL MODEL

A comprehensive model will be developed for a two-link flexible manipulator that undergoes the complete motion regime and will also include all the

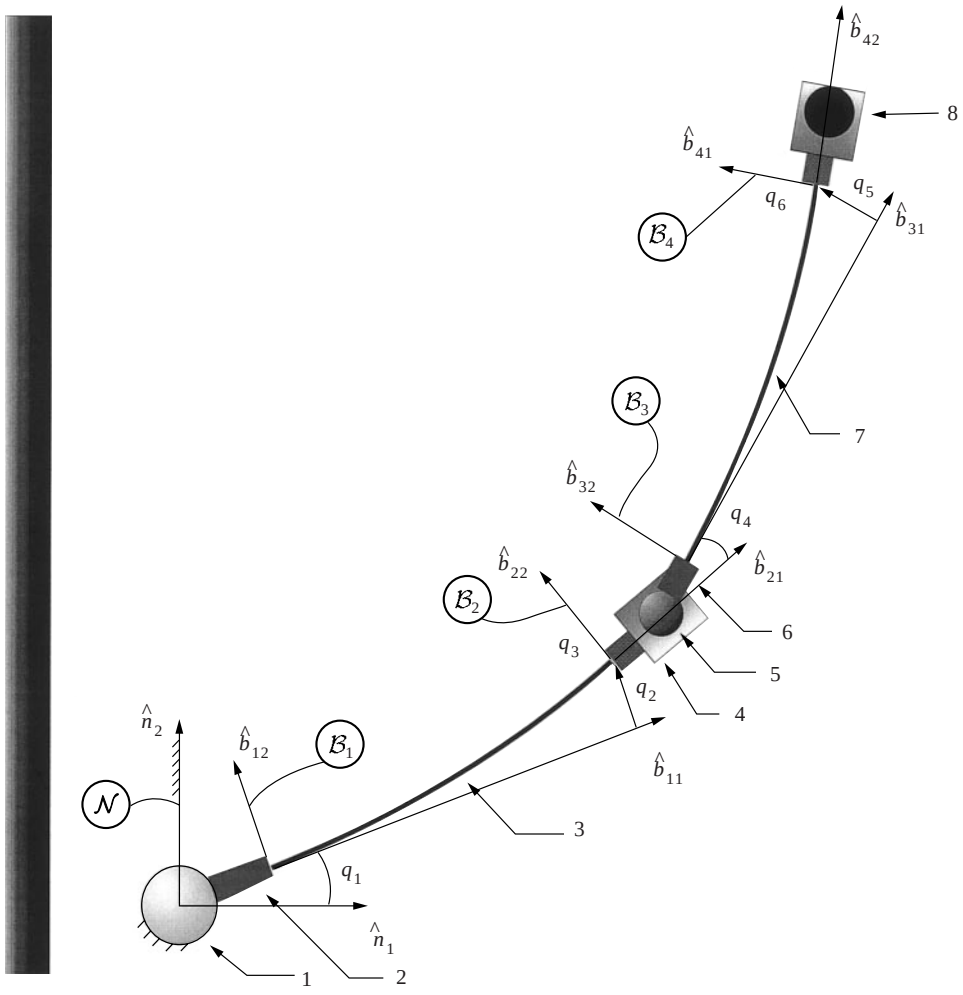

Figure 1. Two-link flexible manipulator in free flight; 1 = *m–g A*, 2 = 1st RB, 3 = 1st EB, 4 = 2nd RB, 5 = *m–g* B, 6 = 3rd RB, 7 = 2nd EB, 8 = 4th RB.

dynamics mentioned above. The schematic of the manipulator in constraint free (free flight) motion is shown in Figure 1, where $q_1(t)$ and $q_4(t)$ are the generalized co-ordinates of the system and the pseudo-co-ordinates [8, 10, 11] $q_2(t)$ and $q_5(t)$ and $q_3(t)$ and $q_6(t)$ are the tip deflections and tip rotations respectively of the two beams. The system considered has four rigid bodies (RB) and two elastic bodies (EB) as shown in Figure 1. The ordinary differential equations governing the two generalized speeds are given by [2, 8–10]

$$\sum_r \left\{ \frac{\partial^o_{\mathcal{N}} \vec{v}^{s_{pr}}}{\partial s_i} \cdot [\vec{F}_r - \vec{I}_r] + \frac{\partial^{\mathcal{N}} \vec{v}^{\mathcal{B}_r}}{\partial s_i} \cdot [\vec{T}_r - \vec{J}_r] \right\} + \sum_e \left\{ \frac{\partial^o_{\mathcal{N}} \vec{v}^{s_{pe}}}{\partial s_i} \cdot [\vec{F}_e - \vec{I}_e] + \frac{\partial^{\mathcal{N}} \vec{v}^{\mathcal{B}_e}}{\partial s_i} \cdot [\vec{T}_e - \vec{J}_e] \right\} = 0, \tag{1}$$

where the subscript r implies the rigid bodies and the subscript e the elastic bodies in the chain of bodies and $i = 1, 4$. The F's and T's are the active forces and torques acting on the bodies and the inertia forces ($\vec{I}_r$) and torques ($\vec{J}_r$) [1, 10] acting on each rigid body of the manipulator are given by

$$\vec{I}_r = m^o_{r\mathcal{N}} \vec{a}^{*_r}, \tag{2}$$

$$\vec{J}_r = {}^{b_{or}}\vec{r}^{*_r} \times m^o_{r\mathcal{N}} \vec{a}^{*_r} + \vec{\vec{I}}_{b_{or}} \cdot {}^{\mathcal{N}}\vec{\alpha}^{B_r} + {}^{\mathcal{N}}\vec{\omega}^{B_r} \times \vec{\vec{I}}_{b_{or}} \cdot {}^{\mathcal{N}}\vec{\omega}^{\mathcal{B}_r}, \tag{3}$$

where r denotes the rth rigid body, and for the elastic bodies by

$$\vec{I}_e = \int_{\Omega_f} m^o_{I_e\mathcal{N}} \vec{a}^{*I_e} \, \mathrm{d}\Omega_e, \tag{4}$$

$$\vec{J}_e = \int_{\Omega_f} [{}^{b_{oe}}\vec{r}^{i_{oe}} \times m^o_{I_e\mathcal{N}} \vec{a}^{*I_e} + ({}^{i_{oe}}\vec{r}^{*I_e} \times m^o_{I_e\mathcal{N}} \vec{a}^{\,i_{oe}} + \vec{\vec{I}}_{i_{oe}} \cdot {}^{\mathcal{N}}\vec{\alpha}^{I_e}_{\mathcal{N}} + {}^{N}\vec{\omega}^{I_e} \times \vec{\vec{I}}_{i_{oe}} \cdot {}^{\mathcal{N}}\vec{\omega}^{I_e})] \, \mathrm{d}\Omega_e, \tag{5}$$

where the equations are written considering a differential slice with inertia per unit domain ($\vec{\vec{I}}_{i_o e}$). The displacement of these beams with respect to their local co-ordinate frame is assumed to conform to field displacements $\tilde{u}_{12}(x_{11}, t)$ for the first beam and $\tilde{u}_{22}(x_{31}, t)$ for the second beam, where

$$\tilde{u}_{12}(x_{11}, t) = \phi_{q_2}(x_{11}) q_2(t) + \phi_{q_3}(x_{11}) q_3(t), \tag{6}$$

$$\tilde{u}_{22}(x_{31}, t) = \phi_{q_5}(x_{31}) q_5(t) + \phi_{q_6}(x_{31}) q_6(t). \tag{7}$$

The shape functions (ϕ_{q_i}) are defined such that they satisfy the geometric boundary conditions and are given by

$$\phi_{q_2}(x_{11}) = \left(\frac{-2x_{11}^3}{L_1^3} + \frac{3x_{11}^2}{L_1^2} \right), \quad \phi_{q_3}(x_{11}) = \left(\frac{x_{11}^3}{L_1^3} - \frac{x_{11}^2}{L_1} \right),$$
$$\phi_{q_5}(x_{31}) = \left(\frac{-2x_{31}^3}{L_2^3} + \frac{3x_{31}^2}{L_2^2} \right), \quad \phi_{q_6}(x_{31}) = \left(\frac{x_{31}^3}{L_2^2} - \frac{x_{31}^2}{L_2} \right), \tag{8}$$

where the x_{i1}'s are as defined in Figure 2. The equations governing the above field displacements are [2, 8–10]

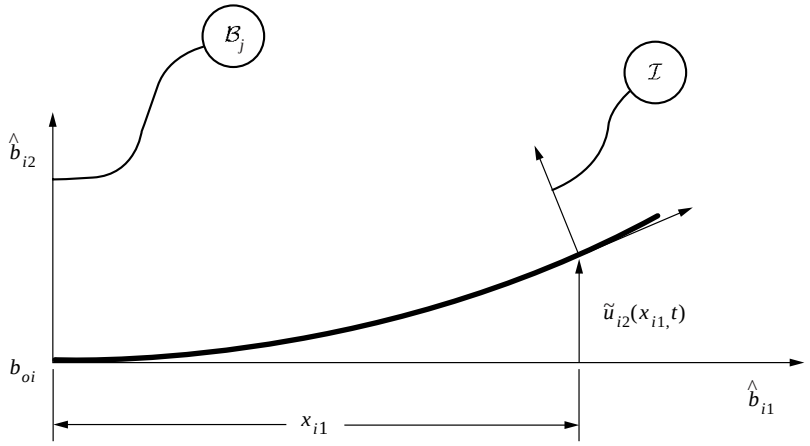

Figure 2. Co-ordinates describing shape of beam.

$$[-m^o_{I_1\mathcal{N}}\vec{a}^{*I_1}]\cdot\frac{\partial^{s_1}_{B_1}\vec{v}^{i_{o1}}}{\partial\dot{\tilde{u}}_{12}(x_{11},\,t)}-\frac{\partial^2}{\partial x^2_{11}}\left(\frac{\partial\bar{V}_1}{\partial\tilde{u}'_{12}(x_{11},\,t)}\right)=0 \tag{9}$$

for the first beam and

$$[-m^o_{I_2\mathcal{N}}\vec{a}^{*I_2}]\cdot\frac{\partial^{s_5}_{B_3}\vec{v}^{i_{o2}}}{\partial\dot{\tilde{u}}_{22}(x_{31},\,t)}-\frac{\partial^2}{\partial x^2_{31}}\left(\frac{\partial\bar{V}_2}{\partial\tilde{u}'_{22}(x_{31},\,t)}\right)=0 \tag{10}$$

for the second beam. The strain energy density function $\bar{V}$ is defined as

$$\bar{V}_i=\frac{1}{2}E_iI_i\left(\frac{\partial^2\tilde{u}_{i2}(x_{i1},\,t)}{\partial x^2_{i1}}\right)^2, \tag{11}$$

where $i=1$ and 2 for the first and second beam, respectively. E_i and I_i are the modulus of elasticity and the area moment of inertia of the respective beams. The boundary conditions for the respective beams are given by equation (1) when the partial velocities are taken w.r.t. $s_2(t)$, $s_3(t)$, $s_5(t)$ and $s_6(t)$ [2, 9]. The weak form (in the sense of Ritz [12]) of equations (9) and (10) yield equations for $s_2(t)$, $s_3(t)$, $s_5(t)$ and $s_6(t)$. The shape functions are used as test functions to generate the weak forms of the field equations. The two ordinary differential equations governing speeds $s_1(t)$ and $s_4(t)$ and the four equations that arise from the field equations along with the six kinematic differential equations comprise the 12 first order differential equations that have to be solved in time to predict the motion of the manipulator in free space. The formulation is expedited via the symbolic tools described by Barhorst [2].

In the case of constrained motion, the typical configuration of the manipulator is as shown in Figure 3. Due to the constraint, the manipulator looses a degree of freedom and hence, $q_4(t)$ is taken to be the dependent co-ordinate. Also, a fictitious co-ordinate $q_7(t)$ is defined which will be used in determining the switching conditions for the motion regimes. With reference to Figure 3, the vector loop equation is written as

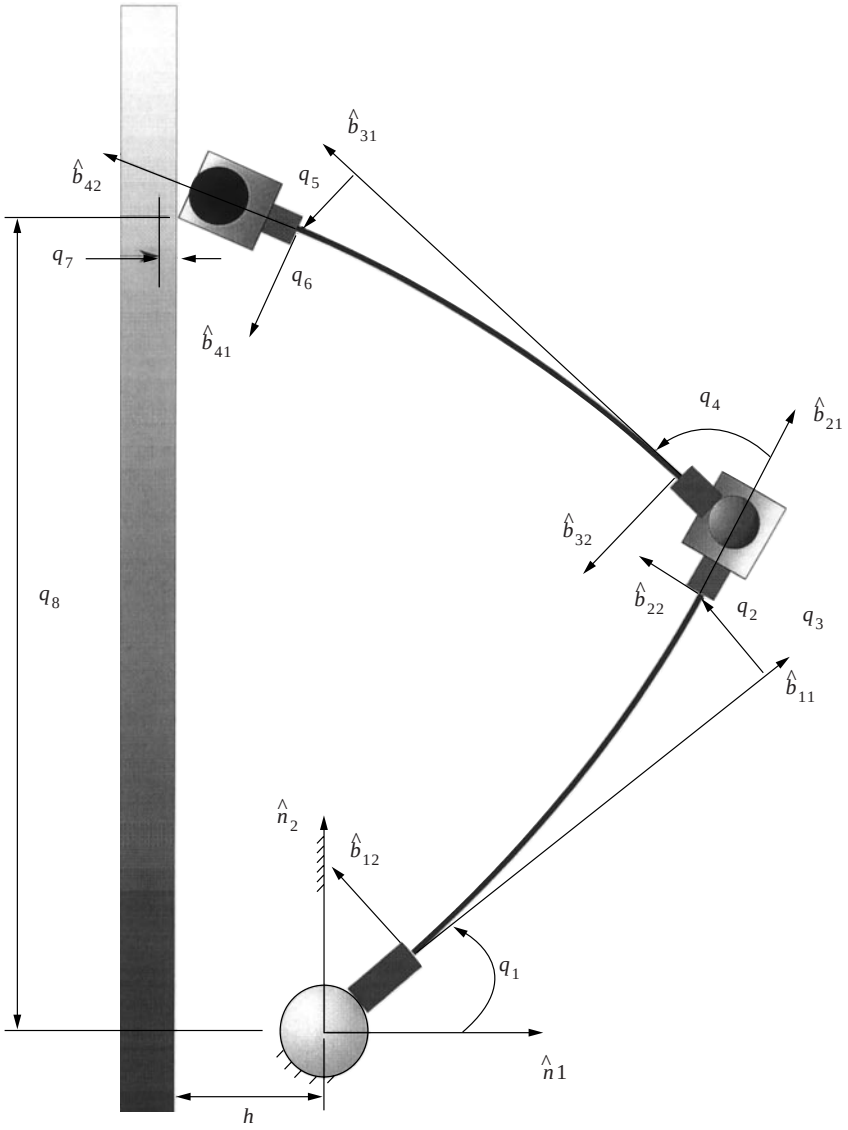

Figure 3. Two-link flexible manipulator in constrained mode.

$$VLE = {}^{o}_{\mathcal{N}}\vec{r}^{*6} + tool_x\hat{b}_{41} + tool_y\hat{b}_{42} - q_7(t)\hat{n}_1 - q_8(t)\hat{n}_2 + h\hat{n}_1 = 0, \qquad (12)$$

where $tool_x$ and $tool_y$ are the distances in the $\hat{b}_{41}$ and $\hat{b}_{42}$ directions respectively to the tip of the tool from the center of gravity of the tip mass. The VLE will be used to solve for $q_4(t)$, the dependent co-ordinate, in terms of the other co-ordinates. To do that, the dot product of equation (12) is taken with vectors $\hat{n}_1$

and $\hat{n}_2$ of $\mathcal{N}$ to get

$$C_1 = VLE \cdot \hat{n}_1 = 0, \quad C_2 = VLE \cdot \hat{n}_2 = 0. \tag{13, 14}$$

The above equations are transcendental and are solved using the Newton–Raphson method. Differentiating equations (13) and (14) w.r.t. time in $\mathcal{N}$ gives

$$\dot{C}_1 = \frac{{}^{\mathcal{N}}\mathrm{d}}{\mathrm{d}t}(VLE \cdot \hat{n}_1) = 0, \quad \dot{C}_2 = \frac{{}^{\mathcal{N}}\mathrm{d}}{\mathrm{d}t}(VLE \cdot \hat{n}_2) = 0, \tag{15, 16}$$

and rearranging the terms results in expressions for the dependent velocities $s_4(t)$ and $s_8(t)$ in terms of the other generalized co-ordinates and speeds as shown below:

$$\begin{Bmatrix} s_4(t) \\ s_8(t) \end{Bmatrix} = \begin{bmatrix} C_{1_{s_4}} & C_{1_{s_8}} \\ C_{2_{s_4}} & C_{2_{s_8}} \end{bmatrix}^{-1} \begin{Bmatrix} rhs_{s_4} \\ rhs_{s_8} \end{Bmatrix} \tag{17}$$

$$= [\mathcal{I}]^{-1} \begin{Bmatrix} rhs_{s_4} \\ rhs_{s_8} \end{Bmatrix}, \tag{18}$$

where $C_{1_{s_4}}$ and $C_{1_{s_8}}$ are the coefficients of $s_4(t)$ and $s_8(t)$ respectively in equation (15) and $C_{2_{s_4}}$ and $C_{2_{s_8}}$ are the coefficients of $s_4(t)$ and $s_8(t)$ respectively in equation (16). Likewise, rhs_{s_4} comprises terms in equation (15) not associated with $s_4(t)$ and $s_8(t)$, and rhs_{s_8} comprises terms in equation (16) not associated with $s_4(t)$ and $s_8(t)$. Similarly, the constrained accelerations $\dot{s}_4(t)$ and $\dot{s}_8(t)$ are given by

$$\begin{Bmatrix} \dot{s}_4(t) \\ \dot{s}_8(t) \end{Bmatrix} = [\mathcal{I}]^{-1} \begin{Bmatrix} rhs_{\dot{s}_4} \\ rhs_{\dot{s}_8} \end{Bmatrix}, \tag{19}$$

where $rhs_{\dot{s}_4}$ consists of terms in $(\mathrm{d}^2/\mathrm{d}^2t)\ C_1 = 0$ not associated with $\dot{s}_4(t)$ and $\dot{s}_8(t)$, and $rhs_{\dot{s}_8}$ consists of terms in $(\mathrm{d}^2/\mathrm{d}^2t)\ C_2 = 0$ not associated with $\dot{s}_4(t)$ and $\dot{s}_8(t)$.

2.1. FORCE OF CONSTRAINT

When the manipulator's tool comes in contact with the constraint surface, the fictitious co-ordinate $q_7(t)$ comes into play. The force, $\vec{F}_c$, that is required to bring the manipulator into conformance with the constraint [9, 11], i.e., for $q_7(t)$ to be zero, is given by equation (1) as

$$\vec{F}_e = \sum_r \left\{ \frac{\partial^o_{\mathcal{N}} \vec{v}^{s_{p_r}}}{\partial s_7} \cdot [\vec{F}_r - \vec{I}_r] + \frac{\partial^{\mathcal{N}} \vec{\omega}^{\mathcal{B}_r}}{\partial s_7} \cdot [\vec{T}_r - \vec{J}_r] \right\} + \sum_e \left\{ \frac{\partial^o_{\mathcal{N}} \vec{v}^{s_{p_e}}}{\partial s_7} \cdot [\vec{F}_e - \vec{I}_e] + \frac{\partial^{\mathcal{N}} \vec{\omega}^{\mathcal{B}_e}}{\partial s_7} \cdot [\vec{T}_e - \vec{J}_e] \right\} \tag{20}$$

i.e., the partial velocities are taken w.r.t. the fictitious speed $s_7(t)$.

Then the manipulator undergoes constrained motion, an opposing force in the form of friction acts on the tool. Hence, the expression for the friction force

acting on that rigid body (namely, the sixth body) is given by

$$(\vec{F}_f)_6 = -\mu(v_{sign})|\vec{F}_c|\hat{n}_2, \tag{21}$$

where μ is the kinetic coefficient of friction and v_{sign} is the sign of the velocity vector of the tip of the tool in constrained motion.

Equation (1) provides the ordinary differential equation of motion in the constrained mode that governs $q_1(t)$ when the quantities† $s_4(t)$ and $\dot{s}_4(t)$ are substituted for from equations (18) and (19), respectively. The partial differential equations (9) and (10) and boundary conditions are valid in the case of constrained motion also when the constrained quantities are rewritten in terms of the independent co-ordinates, velocities and accelerations. Note that in the constrained mode, $q_4(t)$ and $q_8(t)$ are solved using the Newton–Raphson method through transcendental equations (13) and (14) at each time step of the numerical integration process.

2.2. MOMENTUM EQUATIONS ON CONTACT/IMPACT

At the instant the manipulator's tool comes into contact with the constraint surface, a non-holonomic constraint is instantly enforced. This fact is used to derive the post-impact initial conditions for constrained motion. The following equations result in the generalized algebraic momentum equations which, when solved simultaneously, yield post-impact velocities. The algebraic momentum equations for the two-link flexible manipulator are [8, 9]

$$\sum_r \left\{ \frac{\partial {}^o_{\mathcal{N}}\vec{v}^{s_r}}{\partial s_1}\bigg|_{t_o^+} \cdot [\vec{\mathcal{F}}_r - (\vec{L}_r(t_o^+) - \vec{L}_r(t_o^-))] + \frac{\partial {}^{\mathcal{N}}\vec{\omega}^{B_r}}{\partial s_1}\bigg|_{t_o^+} \cdot [\vec{\mathcal{T}}_r - (\vec{H}_r(t_o^+) - \vec{H}_r(t_o^-))] \right\}$$
$$+ \sum_e \left\{ \frac{\partial {}^o_{\mathcal{N}}\vec{v}^{s_e}}{\partial s_1}\bigg|_{t_o^+} \cdot [\vec{\mathcal{F}}_e - (\vec{L}_e(t_o^+) - \vec{L}_e(t_o^-))] + \frac{\partial {}^{\mathcal{N}}\vec{\omega}^{B_e}}{\partial s_1}\bigg|_{t_o^+} \cdot [\vec{\mathcal{T}}_e - (\vec{H}_e(t_o^+) - \vec{H}_e(t_o^-))] \right\}$$
$$= 0 \tag{22}$$

for $s_1(t)$, with

$$[-m_{I_1}({}^o_{\mathcal{N}}\vec{v}^{*I_1}(t_o^+) - {}^o_{\mathcal{N}}\vec{v}^{*I_1}(t_o^-))] \cdot \frac{\partial {}^{s_2}_{\mathcal{B}_1}\vec{v}^{i_{o1}}}{\partial \dot{\tilde{u}}_{12}}\bigg|_{t_o^+} = 0 \tag{23}$$

for $\tilde{u}_{12}(x_{11}, t)$ and

$$[-m_{I_2}({}^o_{\mathcal{N}}\vec{v}^{*I_2}(t_o^+) - {}^o_{\mathcal{N}}\vec{v}^{*I_2}(t_o^-))] \cdot \frac{\partial {}^{s_5}_{\mathcal{B}_3}\vec{v}^{i_{o2}}}{\partial \dot{\tilde{u}}_{22}}\bigg|_{t_o^+} = 0 \tag{24}$$

for $\tilde{u}_{22}(x_{31}, t)$. Equations (23) and (24) are valid pointwise in space.

It should be noted that pre-contact positions are used in calculating the partial velocities in the impact-momentum equations but the post-impact velocity (at time t_o^+) is written to conform to the constrained configuration. The reason being

†These quantities will also be referred to as constrained quantities.

that over the time of impact, the position of the manipulator is considered to remain stationary.

3. NUMERICAL SIMULATION AND EXPERIMENTAL VERIFICATION

The equations of free flight and constrained motion are rearranged to be of the form

$$[I_{ij}]\{\dot{s}_j\} = \{rhs_i\}, \tag{25}$$

where $i = j = 1, 2, \ldots, 12$ for free flight and $i = j = 1, 2, \ldots, 10$ for constrained motion, and the momentum equations in matrix form look like

$$[mom_{ij}]\{s_j\} = \{rhs_{mom_i}\}, \tag{26}$$

where $i = j = 1, 2, \ldots, 5$.

3.1. TORQUE EQUATION

The equation for the torque output of each gearbox was obtained from references [13, 14] as

$$T_i = -J_{eq_i}\dot{s}(t) - C_{eq_i}s(t) + \frac{n_i K_{t_i} e_{a_i}}{R_i} - \frac{n_i^2 K_{t_i} K_{b_i}}{R_i} e_{a_i} s(t), \tag{27}$$

where J_{eq} is the equivalent inertia of the motor and gearbox, C_{eq} is the equivalent damping of the motor and gearbox, K_t is the motor constant, K_b is the back-emf constant, e_a is the applied voltage, n is the gear ratio, and $i = 1$ for the first gearbox and $i = 2$ for the second gearbox. The backlash of the gearboxes was modelled as a deadband.

3.2. EXPERIMENTAL SET-UP

The physical model of the testbed has two permanent magnet DC motors and each drives a planetary gear box. As seen in Figure 4, the first motor–gearbox combination ($m{-}g$ *A*) drives an aluminum beam through a rigid hub (RB_1^3),† as shown in Figure 4. At the end of this beam is a another rigid mass (RB_2) onto which the second motor-gearbox combination ($m{-}g$ *B*) is mounted. A second aluminum beam, has on one end a rigid hub (RB_3) driven by $m{-}g$ *B* and on the other end a tool (RB_4) which impacts with a rigid surface and then moves along the impact surface in the case of constrained motion. The second motor–gearbox combination and the tool are mounted on air bearings which float on an aluminum table 2·5 m long and 1·5 m wide. The angular position of each arm is tracked using digital encoders mounted on the end of the motors. Accelerometers measure the acceleration at various points along the beams, as shown in Figure 4. Two different sets of accelerometers were used. The first set was attached to the mid-point of the beams and had a sensitivity of 100 mV/g and the second set, mounted on the second and fourth rigid bodies, had a

†*RB* implies rigid body.

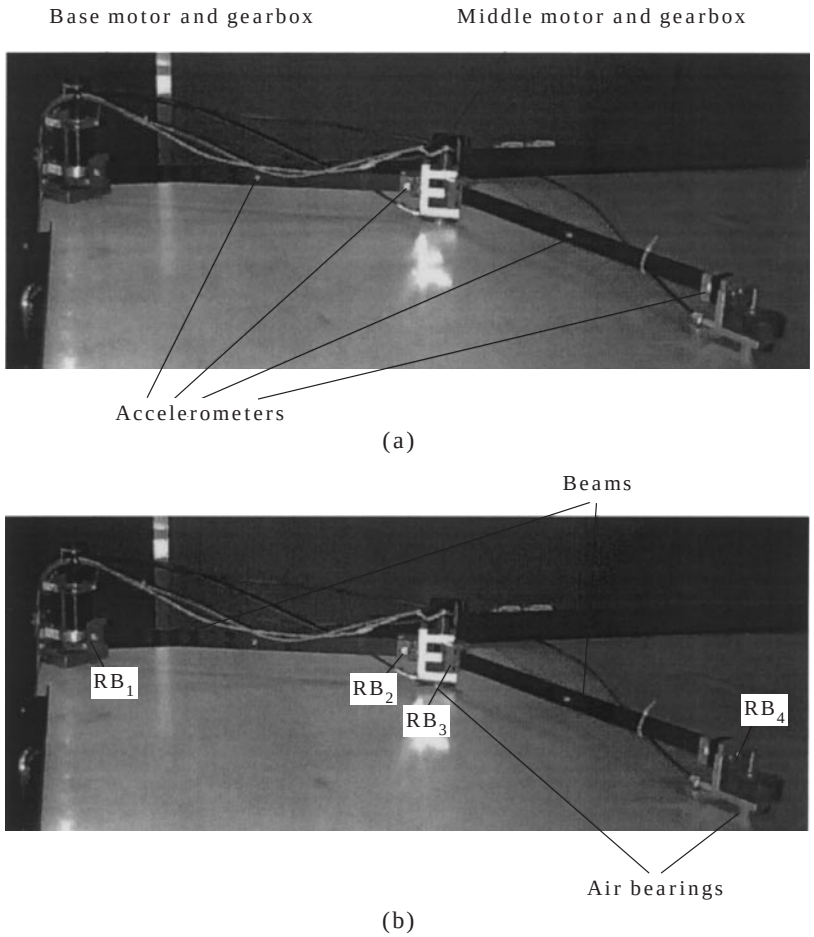

Figure 4. Experimental set-up: (a) accelerometers, (b) beams and air bearings.

sensitivity of 5 mV/g. The motors are powered using a constant voltage DC power supply.

The encoder and accelerometer values were recorded using a Wavebook 512† data acquisition board. This board was connected to a high speed computer which collected the data as each test run was executed. A schematic of the test set-up is shown in Figure 5.

3.3. COMPARISON OF SIMULATION AND EXPERIMENTAL RESULTS

The quantities compared were the angles of the beams ($q_1(t)$ and $q_4(t)$) and the transverse accelerations (in the $\hat{b}_{i2}$ directions) at the mid-point of the two beams and at points on the second and fourth rigid bodies (shown in Figure 4).

†The data acquisition board was made by IOTECH and can record data at a maximum scan rate of 1 MHz.

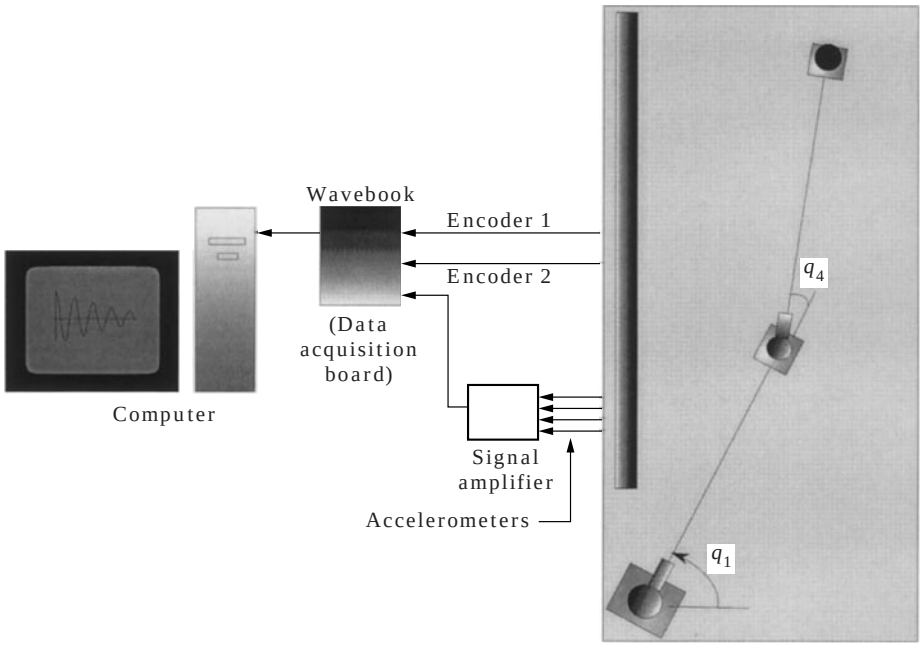

Figure 5. Schematic of data acquisition set-up: arrows indicate direction of data flow.

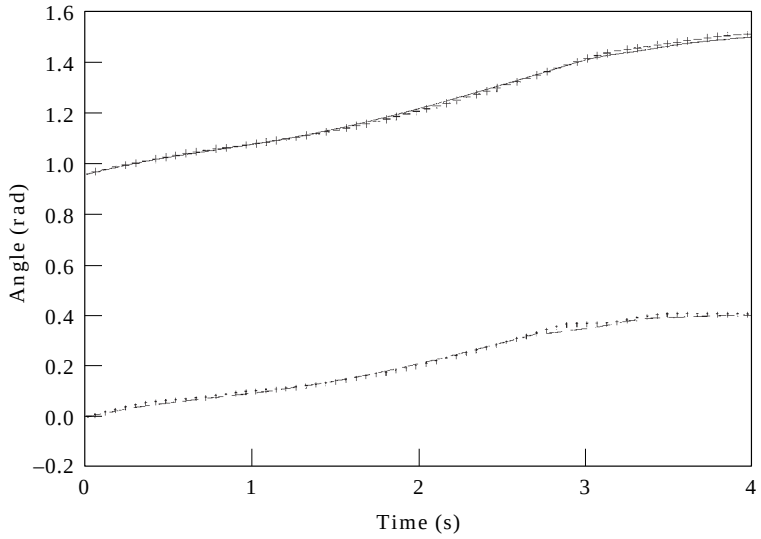

Figure 6. Case 1: plots of angles q_1 (+, experiment; −, simulation) and q_4 (†, experiment; ---, simulation).

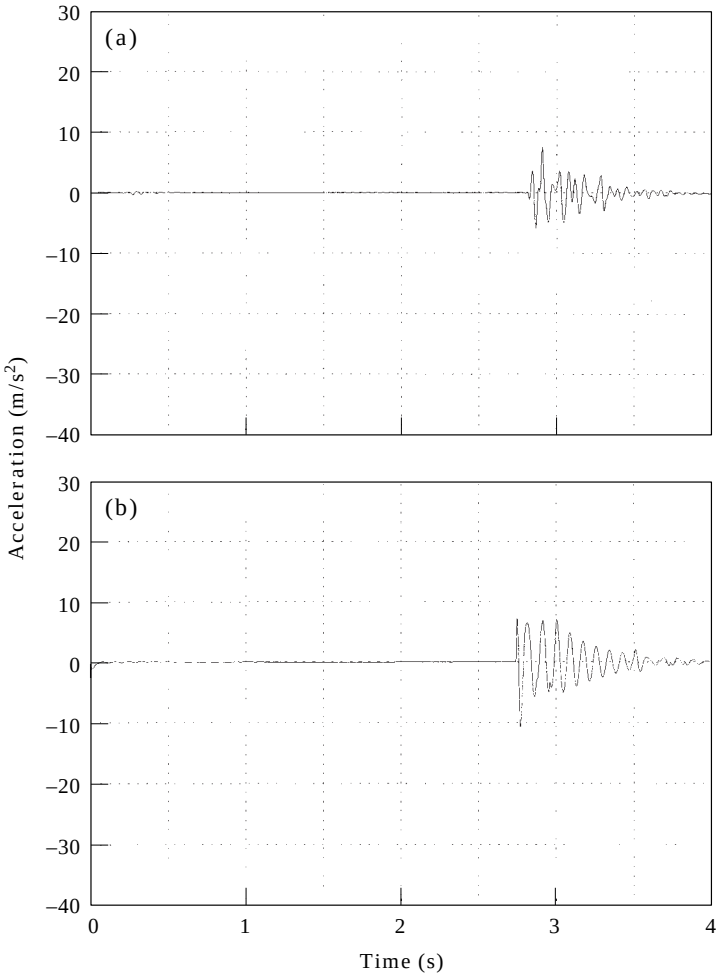

Figure 7. Case 1, plots of acceleration of mid-point of first beam: (a) experiment, (b) simulation.

3.3.1. *Case* 1

In this case, angle $q_1(t)$ was set to 55° and angle $q_4(t)$ to 0°. The base and middle motors were supplied a voltage of 1·5 V and the motion was observed. Figures 7 through 10 show that the calculated accelerations (at the points on the beam mentioned above) match with those measured from the experimental set-up. The results of the simulation and experiment of the two angles mentioned above agree well with each other and are presented in Figure 6.

Two different sets of accelerometers were used to measure accelerations at the beams and rigid bodies. Those mounted on the beams gave relatively better results, i.e., with lesser noise, than those mounted onto the rigid bodies.

In Figure 7, the acceleration at the middle of the first beam is presented from both the experiment and simulation. The two plots in the figure show the basic overall trend. The frequency of the waveform from the experiment and simulation results were 10·96 and 11·53 Hz, respectively. The pre-impact region

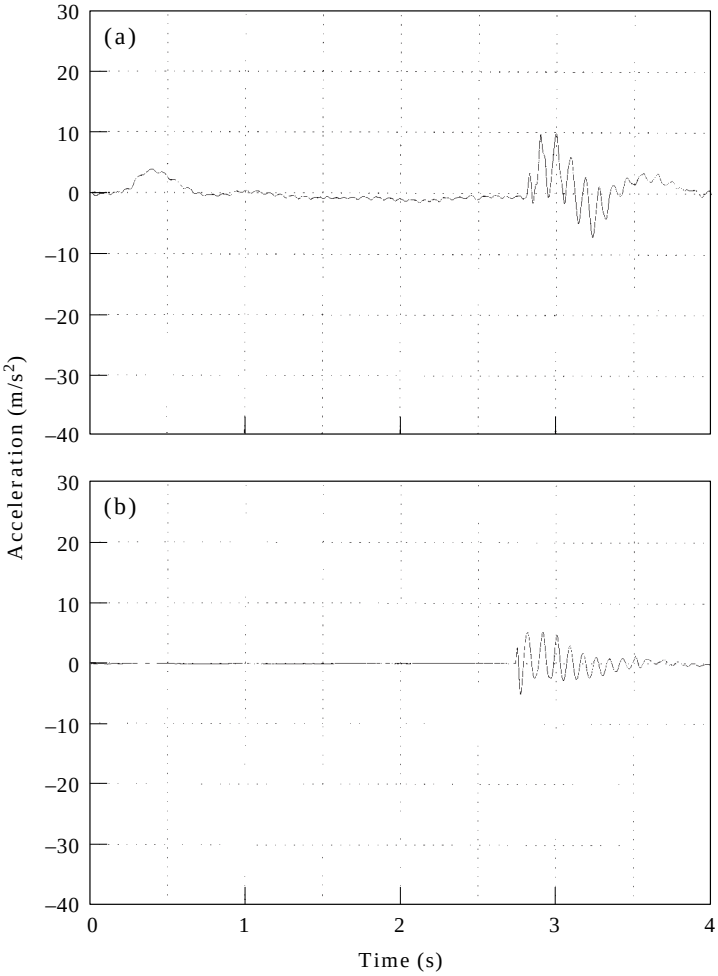

Figure 8. Case 1, plots of acceleration of second rigid body: (a) experiment, (b) simulation.

of both plots show an acceleration of almost zero which is expected as the motion is a constant velocity motion due to a constant voltage applied to the motors. Figure 8 presents the acceleration at the second rigid body. In this case too the frequency of the waveforms match closely. Both plots in Figure 8 show an identical pattern of the overall low frequency waveform. The reason for the higher amplitude of the low frequency waveform in the experimental results was due to a excessive noise in the collected accelerometer data.

The plots in Figure 9 show very good agreement of the results from the simulation and experiment. The frequency of the experimental and simulation waveforms and amplitudes match extremely well. Figure 10 shows the results of the fourth accelerometer on the fourth rigid body. As in the case of the second accelerometer, the free flight portion of the curve shows the result of noisy data. But the frequency of both the experimental and simulation data match. The main reason for the difference in the frequency of the simulation and experiment was the mismatch of the inertia properties of the rigid bodies (since standard

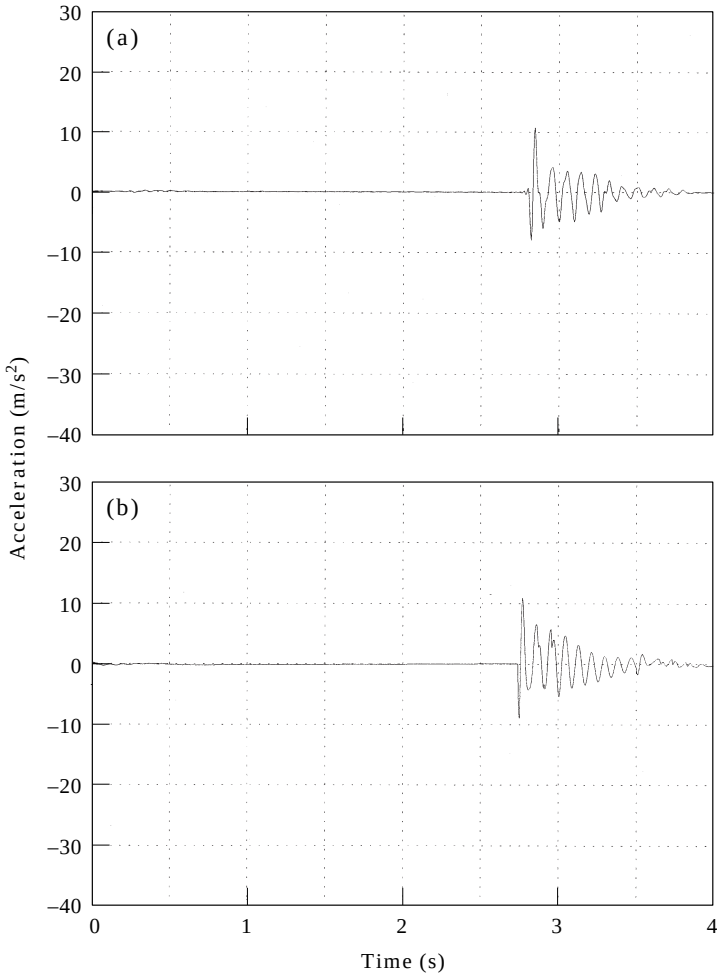

Figure 9. Case 1, plots of acceleration of mid-point of second beam: (a) experiment, (b) simulation.

values of density were used in calculating the mass of each rigid body) and the gearboxes. The time at which impact occurs in the experiment and the simulation differs by 0·07 s. This delay is attributed to the friction between the air bearing and the table, the mismatch of the damping coefficient of the gearboxes and the inertia of the various rigid bodies and gearboxes. The air bearing and the table do not come in contact except at a few high spots on the table. This random friction between the table and the air bearing was not modelled. The damping in the beams was assumed to be proportional to the velocity of their transverse displacement. The effect of this can be seen in the plots as a reasonably smooth exponential decay of the amplitude of accelerations to that of the experimental data. A look at the acceleration data also shows that the damping trends of the simulation results are identical to those of the experiment. Also, the trends at the instant of impact of both the experimental

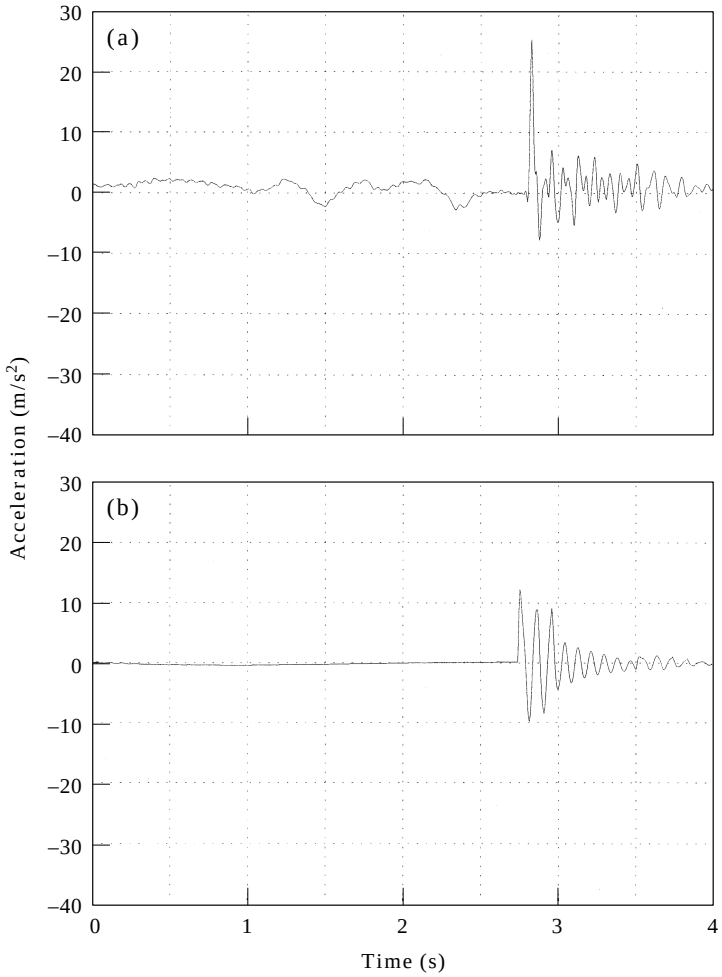

Figure 10. Case 1, plots of acceleration of fourth rigid body: (a) experiment, (b) simulation.

and simulation data are the same, i.e., the acceleration jumps either positive or negative.

A Fast Fourier Transform (FFT) was performed on the raw experimental and simulation data to determine the major frequencies (Figure 13). The difference in these values of frequency mentioned above is mainly due to mismatch of actual and calculated inertia properties of the rigid bodies.

Shown in Figures 11 and 12 are comparisons of snapshots of the actual motion of the two link flexible manipulator captured using a video camera and the animation where the bouncing of the tip from the surface can be clearly seen. The experiment and simulation were performed with the same set of initial conditions and a good agreement between the two can be observed.

3.3.2. *Case* 2

In this case, angle $q_1(t)$ was set to 87° and angle $q_4(t)$ to 0°. The base motor was not supplied any voltage and the middle motor was supplied a voltage of

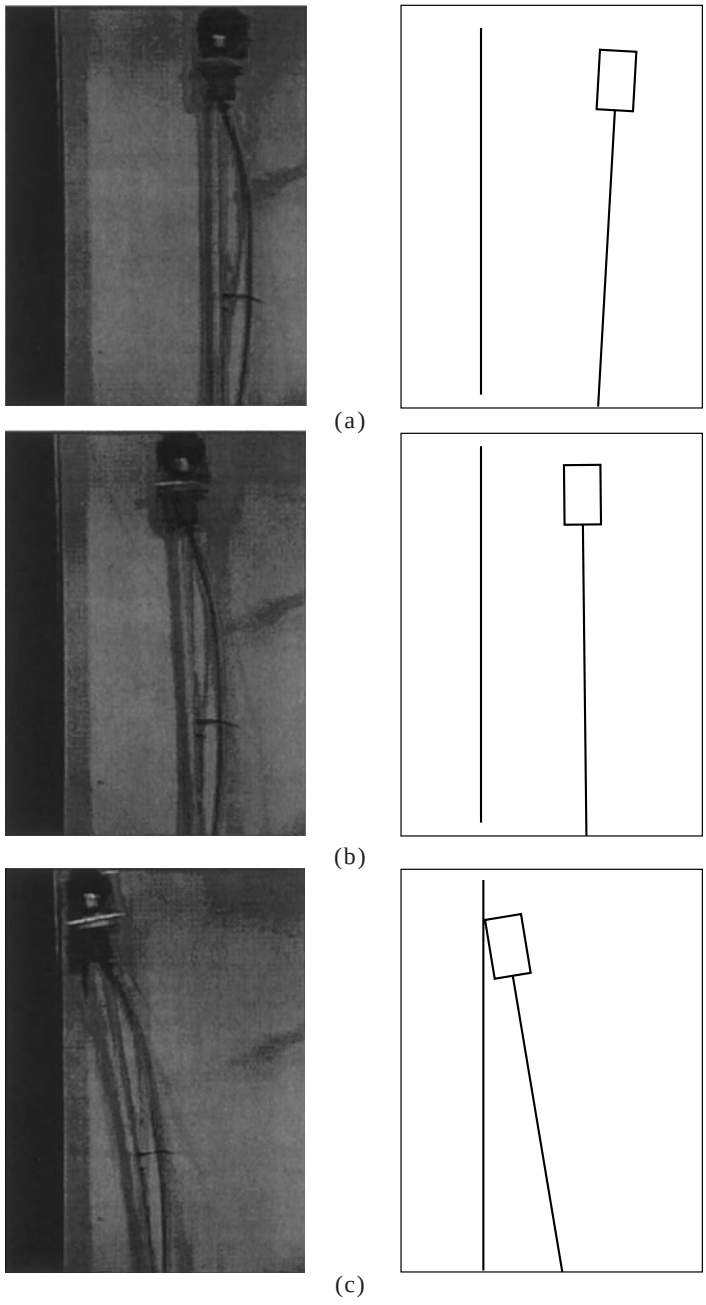

Figure 11. Case 1, comparison of movie and animation: (a) $t = 2{\cdot}12$, (b) $t = 2{\cdot}34$, (c) $t = 2{\cdot}72$.

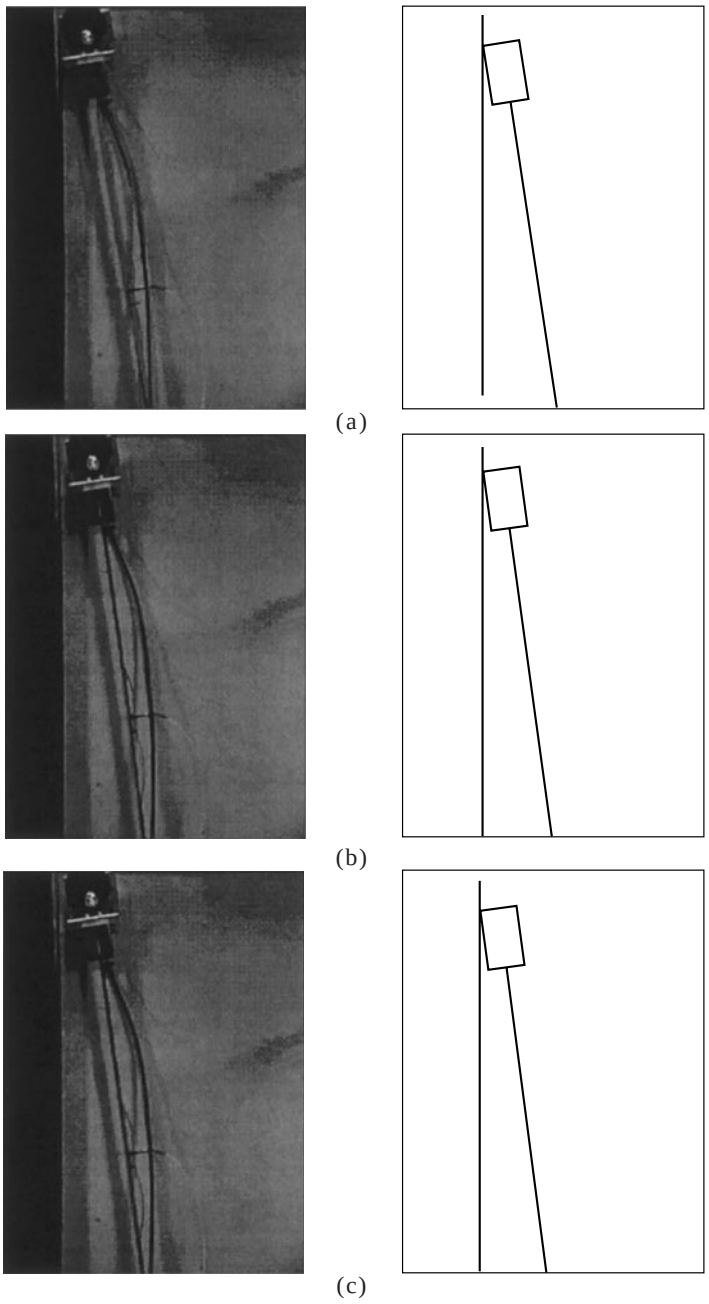

Figure 12. Case 1, comparison of movie and animation: (a) $t = 2{\cdot}81$, (b) $t = 2{\cdot}97$, (c) $t = 3{\cdot}44$.

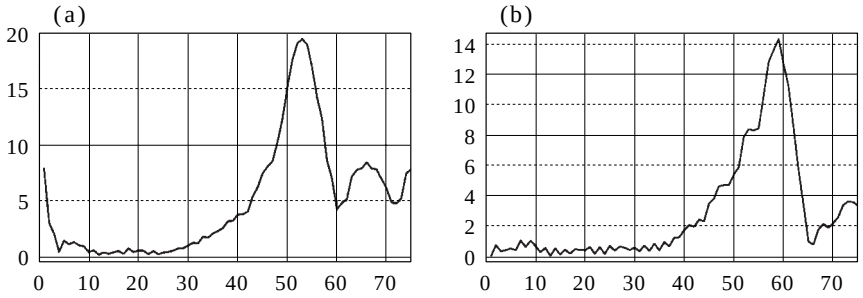

Figure 13. Case 1, comparison of FFT of experimental and simulation acceleration data at mid-point of first beam: (a) experimental, $f = 10{\cdot}96$; (b) simulation, $f = 11{\cdot}59$.

1·5 V and the motion along the constraint surface was observed. The plots of angles $q_1(t)$ and $q_4(t)$ for the simulation and experiment are shown in Figure 14 and those for acceleration in Figures 15 and 16.

The simulation and experimental results for angle $q_1(t)$ in Figure 14 do not match as closely as they do for angle $q_4(t)$. The reason for this is that in this configuration, due to the uneven distribution of the load over the middle air bearing, it tips over and binds with the table.

As in Case 1, the major trends, the overall waveform and overall frequency in the experimental and simulation results match closely. The difference in time of impact and frequencies in the experiment and simulation are once again attributed to the reasons discussed in Case 1.

3.3.3. *Case* 3

In order to demonstrate the model's applicability to control and to illustrate the model's ability to go through the complete motion regime seamlessly, a

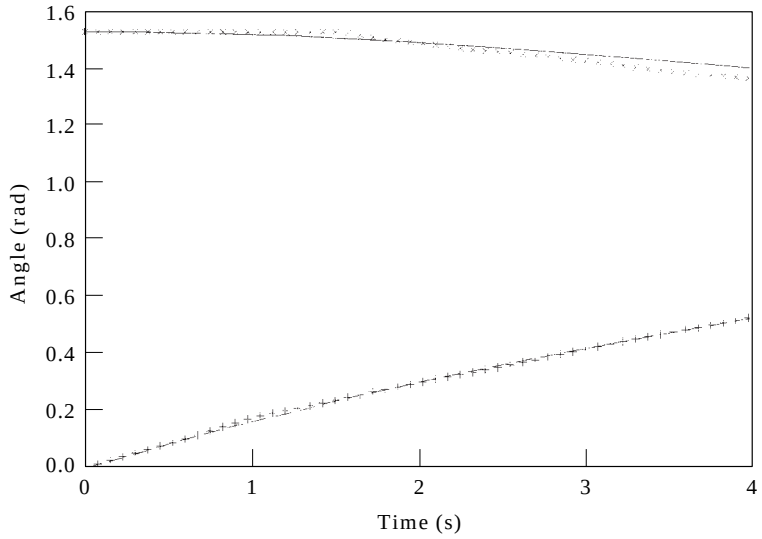

Figure 14. Case 2, plots of angles q_1 ($\times$, experiment; $-$, simulation) and q_4 ($+$, experiment; ---, simulation).

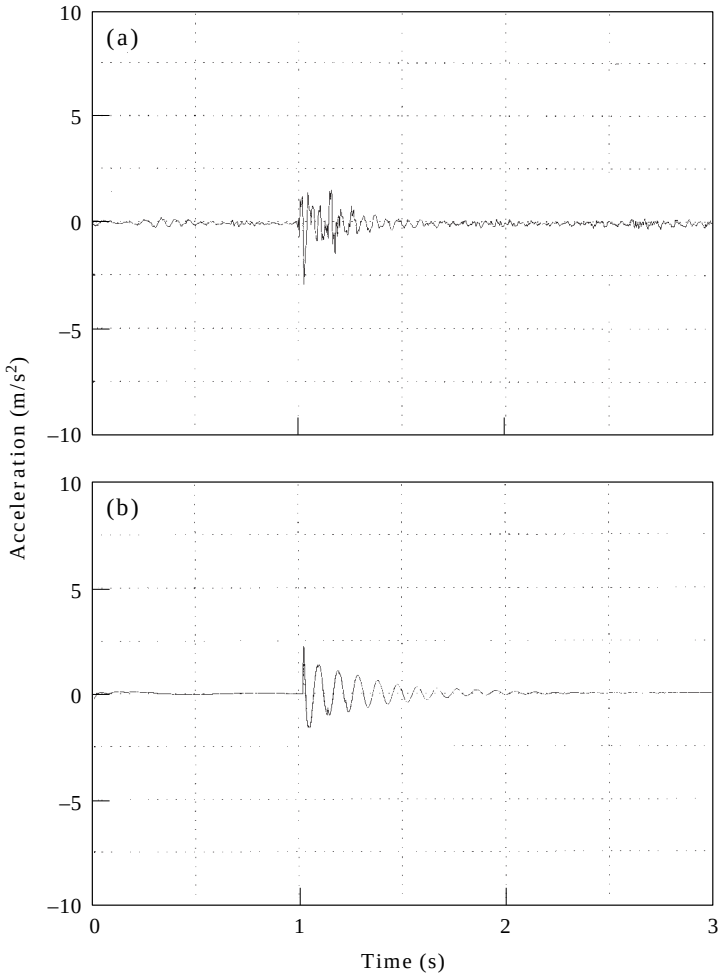

Figure 15. Case 2, plots of acceleration of mid-point of first beam: (a) experiment, (b) simulation.

sanding like operation was simulated where the tip of the manipulator is forced to move along the constraint surface by varying the commanded position of the tip in time. A simple proportional control law was proposed to implement the sanding operation where the tip of the manipulator was commanded to move along the constraint surface in a cyclic fashion. We did not model the possibility of the tool sticking to the workpiece. However, this stiction effect can easily be modelled using the techniques herein, and will be included in models for further studies. Even without stiction explicitly modelled, we do get interesting dynamics induced by friction.

It is interesting to note from Figures 17 and 18 that the manipulator realizes the full motion regime. Figure 17 shows the position of the tip of the manipulator in the $\hat{n}_1$ or x-direction, and Figure 18 the plot of x versus y position of the tip of the manipulator.

The constraint surface is 25 mm in the negative $\hat{n}_1$ direction. The above plots show the time and position at which the tip leaves the surface. An effect of

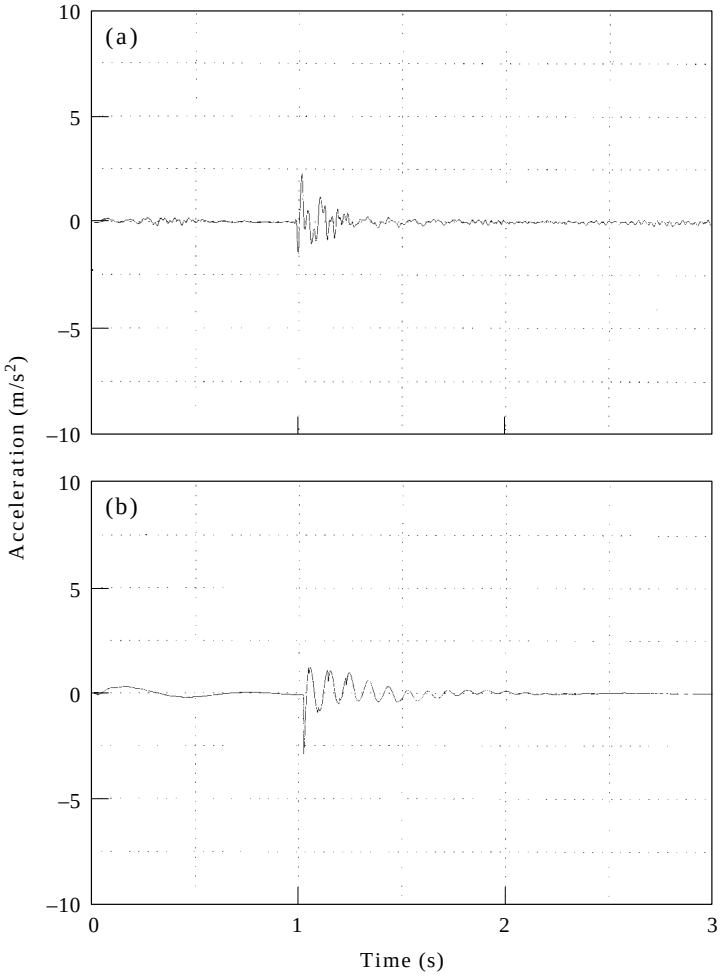

Figure 16. Case 2, plots of acceleration of mid-point of second beam: (a) experiment, (b) simulation.

impact with friction that the model was able to predict was direction reversal. This effect is well noticed in the animation but can also be noticed in the plot of the tip position in the x direction at time $t = 2{\cdot}25$ s.

4. SUMMARY

In this paper, a model based on the methodology presented by Barhorst that undergoes the complete motion and incorporates all the dynamics listed in the introduction was developed and completely verified. The verification was done via an experimental set-up of a planar two-link flexible manipulator described in section 3.2. The plots of the angles of the two beams, accelerations of the rigid bodies and mid-points of the two beams and comparison of the animation of the two-link flexible manipulator and the video of the motion of the test set-up were presented to validate the verification of the model and the methodology.

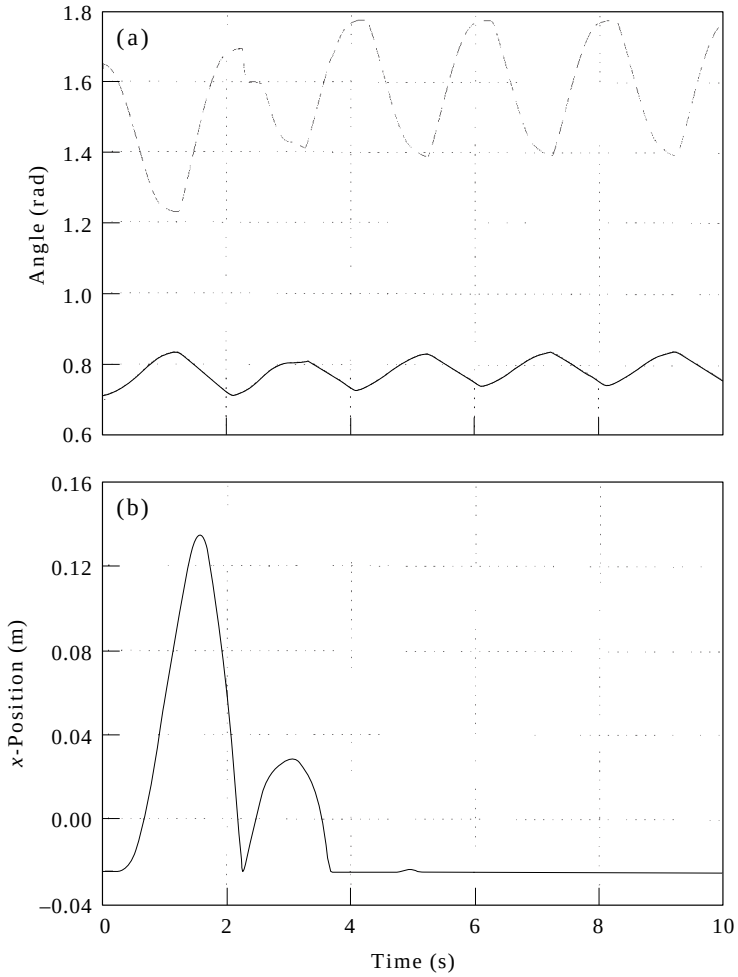

Figure 17. Demonstration of control: (a) plot of angles (---, q_1; —, q_2) and (b) x-position of tip of flexible manipulator (sanding operation).

Moreover, the model included realistic effects like motor dynamics, gearbox dynamics, backlash from the gearboxes, friction on impact and in constrained motion and the effect of all interconnecting rigid bodies. Also, the resulting set of equations was the minimal set and the impact process was modelled without the use of a coefficient of restitution and the contact constraints were completely satisfied.

Comparisons of the simulation with the motion of the actual system were provided to show that the model predicted the impact process accurately. With only six degrees of freedom, the model manifested the complete dynamics of the manipulator. The adaptability of the model for control applications was demonstrated through Case 3.

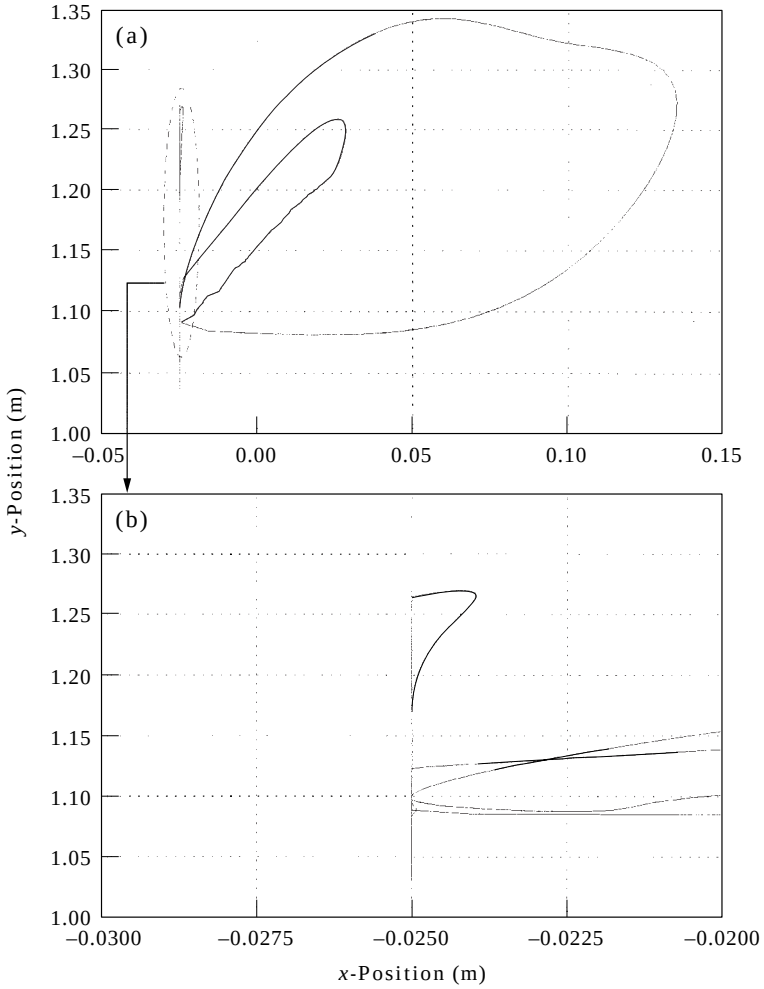

Figure 18. Demonstration of control: (a) plot of *xy*-position of tip of flexible manipulator (sanding operation), (b) data: 1.

REFERENCES

1. A. A. BARHORST and L. J. EVERETT 1995 *The International Journal of Nonlinear Mechanics* **30**, 1–21. Modeling hybrid parameter multiple body systems: a different approach.
2. A. A. BARHORST 1997 *Journal of Sound and Vibration* **208**, 823–839. Symbolic equation processing utilizing vector/dyad notation.
3. R. M. BRACH 1993 *International Journal of Impact Engineering* **13**, 21–33. Classical planar impact theory and the tip impact of a slender rod.
4. W. J. STRONGE 1990 *Proceedings of Royal Society of London A* **431**, 169–181. Rigid body collisions with friction.
5. D. STOIANOVICI and Y. HURMUZULU 1996 *Journal of Applied Mechanics* **63**, 307–316. A critical study of the applicability of rigid-body collision theory.
6. Q. H. QIN and X. Q. HE 1995 *Computer Methods in Applied Mechanics and Engineering* **122**, 205–222. Variational principles, fe and mpt for analysis of nonlinear impact-contact problems.
7. I. HUNEK 1993 *Computers and Structures* **48**, 193–203. On a penalty formulation for contact–impact problems.

8. A. A. BARHORST and L. J. EVERETT 1993 *Journal of Dynamic Systems, Measurement and Control* **117**, 559–569. Contact/impact in hybrid parameter multiple body mechanical systems.
9. A. A. BARHORST 1998 *Journal of Sound and Vibration* **209**, 571–592. On modeling variable structure dynamics of hybrid parameter multiple body systems.
10. A. A. BARHORST and L. J. Everett 1992 In *Proceedings of the ASME Symposium on Dynamics of Flexible Multibody Systems: Theory and Experiment, Anaheim, CA*, 197–205. A methodology for modeling hybrid parameter multiple body systems.
11. T. R. KANE and D. A. LEVINSON 1985 *Dynamics: Theory and Application*. McGraw Hill Series in Mechanical Engineering. New York: McGraw-Hill.
12. J. N. REDDY 1984 *Energy and Variational Methods in Applied Mechanics*. New York: Wiley.
13. J. J. D'AZZO and C. H. HOUPIS 1981 *Linear Control System Analysis and Design*. New York: McGraw-Hill; 2nd edition.
14. R. M. KLOECKER 1992 *Master's thesis, Michigan Technological University*. Analysis and simulation of the combined effects of non-linear friction and gear backlash on an electromechanical position control system.

APPENDIX: NOMENCLATURE

${}^{A}\vec{\omega}^{B}$	angular velocity of frame B in frame A (the uppercase superscript denotes a frame of reference)
${}^{A}\vec{\alpha}^{B}$	angular acceleration of frame B in frame A
${}^{a}\vec{r}^{b}$	position vector from point a (tail) to point b (head) (the lowercase superscript denotes a point)
${}^{i_{oe}}\vec{r}^{*I_e}$	position of c.g. of differential slice of elastic body in its local co-ordinate system
${}^{A}\mathrm{d}/\mathrm{d}t$	differentiation w.r.t. reference frame A
$({}^{A}\mathrm{d}/\mathrm{d}t){}^{a}\vec{r}^{b} = {}^{o}_{A}\vec{v}^{b}$	velocity of point b relative to point a as seen in reference frame A
$({}^{A}\mathrm{d}/\mathrm{d}t){}^{a}\vec{v}^{b} = {}^{o}_{A}\vec{a}^{b}$	acceleration of point b relative to point a as seen in reference frame A
${}^{o}_{\mathcal{N}}\vec{a}^{\,i_{oe}}$	absolute acceleration of origin of co-ordinate system associated with elastic body e
${}^{o}_{\mathcal{N}}\vec{a}^{*I_e}$	absolute acceleration of differential slice of elastic body e
$\bar{V}$	strain energy density function (scalar)
$\vec{F}$, $\vec{T}$	applied forces (F) and torques (T)
m_r	mass of rigid body r
m_{I_e}	mass per unit domain of elastic body e
$\vec{\vec{I}}_{b_{or}}$	inertia dyad of rigid body (r)
$\vec{\vec{I}}_{I_{oe}}$	inertia dyad per unit domain of elastic body (e)
$\vec{L}_i$	linear momentum of rigid ($i = r$) or elastic ($i = e$) body
$\vec{H}_i$	angular momentum of rigid ($i = r$) or elastic ($i = e$) body
$\vec{\mathcal{F}}_i$	resultant active impulse of force on rigid ($i = r$) or elastic ($i = e$) body

$\vec{\mathcal{T}}_i$ non-constraint impulsive moments including impulses of couples about point S_{p_i} ($i = r$ or e for rigid or elastic bodies, respectively)

S_{p_i} special point associated with each rigid ($i = r$) or elastic ($i = e$) body in the system of bodies